

DWTNeRF: Boosting Few-shot Neural Radiance Fields via Discrete Wavelet Transform

Hung Nguyen Runfa Blark Li Truong Nguyen
Video Processing Lab, UC San Diego
{hun004, runfa, tqn001}@ucsd.edu

Abstract

Neural Radiance Fields (NeRF) has achieved superior performance in novel view synthesis and 3D scene representation, but its practical applications are hindered by slow convergence and reliance on dense training views. To this end, we present DWTNeRF, a unified framework based on Instant-NGP’s fast-training hash encoding. It is coupled with regularization terms designed for few-shot NeRF, which operates on sparse training views. Our DWTNeRF additionally includes a novel Discrete Wavelet loss that allows explicit prioritization of low frequencies directly in the training objective, reducing few-shot NeRF’s overfitting on high frequencies in earlier training stages. We also introduce a model-based approach, based on multi-head attention, that is compatible with INGP, which are sensitive to architectural changes. On the 3-shot LLFF benchmark, DWTNeRF outperforms Vanilla INGP by 15.07% in PSNR, 24.45% in SSIM and 36.30% in LPIPS. Our approach encourages a re-thinking of current few-shot approaches for fast-converging implicit representations like INGP or 3DGS.

1. Introduction

NeRF [21] have emerged as a powerful method for reconstructing 3D scenes from a set of 2D images. This can generate photorealistic views from novel angles. Its properties have enabled applications in medical imaging [4, 5], robotics [44, 45], virtual reality [36, 38], autonomous driving [19, 32], and many more.

However, a disadvantage of NeRF is its slow convergence, which can take several hours to render a scene [28]. Besides, it requires a dense set of training views [29]. Those problems can hinder NeRF’s practical uses. For the former problem, INGP [22] introduced a multi-resolution hash encoding that dramatically reduces training time. However, to the best of our knowledge, limited research has been conducted on few-shot INGP. Therefore, our work will focus on addressing this gap.

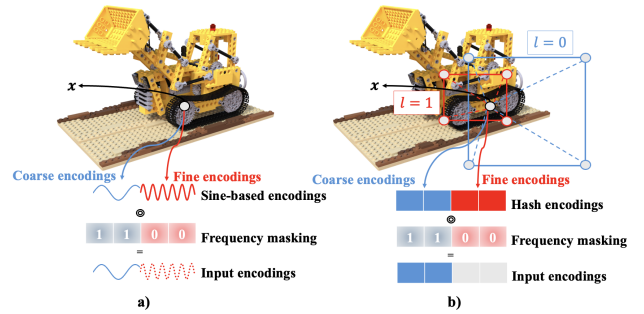


Figure 1. Comparison of frequency masking as applied to sine-based encoding (a) and multi-resolution hash encoding (b). To be compatible with frequency masking [39], the later portions of the encoded inputs $\gamma(\mathbf{x})$ must strictly correspond to high frequencies. For the hash encoding, those input portions correspond to fine resolutions, which are not interchangeable with high frequencies.

INGP has distinct characteristics that make some recent few-shot approaches incompatible. Firstly, its positional encoding is based on multi-resolution. This differs from the sine-based encoding [26] in Vanilla NeRF and similar works, which *explicitly* map inputs to high frequencies for learning intricate details. The sine-based encoding supports frequency masking [39], a regularization strategy that element-wise masks high-frequency inputs early in training to prevent overfitting. However, applying this to INGP, as in Figure 1, assumes fine resolutions correspond to high frequencies, which is not strictly true. For instance, a point on a flat, monochromatic surface remains low frequency, irrespective of resolution. We will show in Section 5.4 that rendering improvements can be achieved just by removing frequency masking from INGP.

Secondly, INGP is fast-converging. Its aggressive optimization dynamics amplify the impact of even small adjustments. This is a challenge for model-based methods, which focus on tweaking the Vanilla MLP’s architecture in NeRF to improve its few-shot capabilities [46]. We will again show

in Section 5.4 that slight architectural changes, like simply adding *one* more layer and some residual connections, degrade few-shot INGP’s performance.

The above discussion yields a two-fold motivation. Firstly, given the proven effectiveness of frequency-based regularization, we need to devise a method that accomplishes the same idea, but compatible with INGP. To this end, we decompose the rendered and ground-truth scenes into levels of frequencies, using the Discrete Wavelet Transform. Their frequency-space differences are minimized by our novel Discrete Wavelet loss. By setting a higher weight to low-frequency discrepancies, we can *explicitly* prioritize their learning right in the training objective. Secondly, given the proven effectiveness of model-based methods, we need to devise a method that does not degrade INGP, which is sensitive to architectural changes. Our focus is on modelling the color-density interactions. While better modelled with separate MLP branches, they still require some levels of interactions [46]. We call this the “cross-branch interactions”. To this end, we propose using multi-head attention modules at the input and output levels. This does not incur architectural changes to the MLP, and does not degrade performance like other model methods.

In summary, our contributions are as follows:

- A unified framework, DWTNeRF, that blends the following prevalent approaches towards few-shot INGP:
- *Regularization-based* approach with a novel Discrete Wavelet loss that explicitly decomposes the scenes into low and high-frequencies, enabling prioritizing low frequencies at earlier training stages;
- *Model-based* approach to enable cross-branch interactions using multi-head attention, which is compatible with fast-converging INGP;
- Through comprehensive experiments, we demonstrate that the proposed DWTNeRF is highly competitive with state-of-the-art methods, especially under highly challenging 2- to 4-shot conditions. The proposed DWTNeRF is also much faster due to being INGP-based.

2. Related Works

2.1. Neural Radiance Fields

NeRF [21] has attained wide popularity in novel view synthesis and 3D scene representation tasks. It is self-supervised, able to construct 3D scenes without any 3D ground-truth data, relying only on multi-view images. Compared to earlier view synthesis methods, it is highly photorealistic. However, Vanilla NeRF is limited in practical applications [7]. Therefore, further research has been aimed at faster training & rendering [41], generalizability [40], dynamic scenes [25], 3D generation [12], etc. In the sub-field of fast-training NeRF, INGP [22] introduced a multi-resolution hash encoding whose CUDA implementation can render scenes within

seconds. On top of INGP, we focus on another sub-field: few-shot NeRF, which aims to reduce its high dependence on a dense training set of multi-view images.

2.2. Few-shot NeRF

Prior-based methods Those enable few-shot NeRF by training a generalized model on a large dataset of diverse scenes or by incorporating pre-trained priors in their training objectives. pixelNeRF [42] leveraged a feature encoder to extract image features from sparse input views, and conditioned a NeRF on these features. DietNeRF [11] introduced a semantic consistency loss that minimizes discrepancies in embeddings of rendered and ground-truth views, encouraging high-level semantic similarities. RegNeRF [23] leveraged a trained normalizing flow model to regularize color patches of unobserved views. SparseNeRF [8] introduced a local depth ranking loss based on priors from a trained depth estimation model. SPARF [33] minimized coordinate-space discrepancies between pixel matches in multiple ground-truth views, predicted by a trained feature matching model. This encourages a global and geometrically accurate solution. GeCoNeRF [17] extended this concept of geometric consistency to the feature-space, regularizing both semantically and structurally.

Regularization-based methods Those enable few-shot NeRF by additionally introducing regularization terms, optimizing in a per-scene manner. InfoNeRF [16] introduced a KL-divergence loss that enforces consistent density distributions across neighboring rays. RegNeRF [23] introduced a depth smoothness loss that penalizes depth discrepancies between neighboring points. Mip-NeRF 360 [1] introduced a distortion loss that reduces floating artifacts by minimizing the weighted distances between sampled points. DiffusionNeRF [37] introduced a full geometry loss that encourages the weights of sampled points along each ray to sum to unity, which ensures the rays are absorbed fully by the scene’s geometry. Another significant work is FreeNeRF [39], which did not introduce new terms but proposed masking input encodings in a coarse-to-fine manner, preventing NeRF from overfitting on high frequencies in early training stages. CombiNeRF [2], which our work is based on, synergistically combined all these techniques on top of INGP, achieving SOTA results.

Model-based methods [46] shows that Vanilla MLP is not sufficient for few-shot NeRF. They introduced two main modules, which we term “Residual Connections” and “Element-wise Cross-branch Interactions”. In the former, the encoded inputs are fed into each MLP layer, ensuring a shorter connection between the inputs and outputs. This is similar to ResNet [9] & DenseNet’s [10] residual connections. In the latter, the colors & densities are modeled using separate MLP branches, and cross-branch interactions are learned by a simple element-wise addition between cor-

responding layers. This pioneering work presented a new direction towards few-shot NeRF: adjusting Vanilla MLP’s architecture.

However, aside from DiffusioNeRF and CombiNeRF, none of the works above are based on INGP. Our experiments reveal that not all few-shot methods are transferable across Vanilla NeRF and INGP. Precisely, frequency regularization and model-based approaches are not trivially transferable. This is due to INGP’s multi-resolution encoding and fast convergence, as explained in Section 1. To this end, we present a blend of regularization- and model-based approaches that are INGP-compatible.

3. Preliminaries

3.1. Neural Radiance Fields

NeRF optimizes a 5D plenoptic function that represents a 3D volume, $f(\mathbf{x}, \mathbf{d})$, where $\mathbf{x} = (x, y, z)$ is a 3D spatial position viewed from a unit direction $\mathbf{d} = (\theta, \phi)$. f outputs a view-dependent RGB color \mathbf{c} and a differential volume density σ , parameterized by an MLP. To calculate the colors in a pixel grid, we start by shooting a ray $\mathbf{r}(t)$ into the 3D scene, through a pixel \mathbf{p} . The ray has an origin at \mathbf{o} and a 3D direction \mathbf{d} . Along the ray, we sample multiple points. f learns the color \mathbf{c} and the density σ of each point. The final color of the pixel \mathbf{p} , $\mathbf{c}(\mathbf{r})$, is calculated with simplified volume rendering [13]:

$$\mathbf{c}(\mathbf{r}) = \int_{t_n}^{t_f} T(t) \sigma(\mathbf{r}(t)) \mathbf{c}(\mathbf{r}(t), \mathbf{d}) dt \quad (1)$$

where t_n and t_f denote the lower and higher-bound spatial positions of the sampled points. The color of a point t is $\mathbf{c}(\mathbf{r}(t), \mathbf{d})$, weighted by the point’s density $\sigma(\mathbf{r}(t))$. This is again weighted by the transmittance $T(t)$, the exponential of the negative integral of the differential density. It can be interpreted as the probability that the ray traverses uninterrupted from t_n to t [24]. The process repeats for all rays forming a batch \mathcal{R} . NeRF is optimized by minimizing the MSE between predicted colors $\mathbf{c}(\mathbf{r})$ and ground-truth colors $\mathbf{c}_{gt}(\mathbf{r})$, under the same pose \mathbf{p} :

$$\mathcal{L}_{MSE} = \frac{1}{|\mathcal{R}|} \sum_{\mathbf{r} \in \mathcal{R}} \|\mathbf{c}(\mathbf{r}) - \mathbf{c}_{gt}(\mathbf{r})\|_2^2$$

3.2. Discrete Wavelet Transform (DWT)

Here, we explain the DWT, which our Discrete Wavelet loss (Section 4.2) is based on. Suppose that the ray batch \mathcal{R} consists of adjacently sampled rays \mathbf{r} . This amounts to a 2D image \mathbf{I} , which can be compared with the ground-truth image \mathbf{I}_{gt} . We can perform the DWT on \mathbf{I} to receive the four following sub-bands:

$$\mathbf{I}^{LL} = \mathbf{LIL}^T; \mathbf{I}^{LH} = \mathbf{HIL}^T$$

$$\mathbf{I}^{HL} = \mathbf{LIH}^T; \mathbf{I}^{HH} = \mathbf{HIH}^T$$

where \mathbf{L} and \mathbf{H} are the low- and high-pass 2D matrices, respectively. \mathbf{L} is constructed with shifting rows of its corresponding 1D low-pass wavelet filter ℓ , and similarly for \mathbf{H} . If ℓ is orthogonal, then the 1D high-pass filter h is derived trivially from ℓ , and \mathbf{H} trivially from \mathbf{L} [30]. \mathbf{I}^{LL} is called the LL sub-band of \mathbf{I} , and so on for other components. Intuitively, \mathbf{I}^{LL} represents the low-frequency components of the image. \mathbf{I}^{LH} and \mathbf{I}^{HL} represent high frequencies in one direction, but low frequencies in another. Finally, \mathbf{I}^{HH} represents the high frequencies in both vertical & horizontal directions. Because \mathbf{L} is constructed with shifting rows of ℓ (and similarly for \mathbf{H}), the sub-bands are only a quarter of the original image. This is a concern in applying the DW loss, which we will explain later.

4. Methodology

4.1. Overview

Figure 2 shows the architecture diagram of our DWTNeRF. It consists of two main modules: the Discrete Wavelet (DW) loss and cross-branch interactions. The DW loss decomposes rendered and ground-truth views into levels of frequencies, and minimizes the differences in their frequency representations. By setting a higher weight for low-frequency differences, we can explicitly prioritize them in earlier training stages, thereby reducing overfitting on high frequencies. This represents a *regularization-based* approach that is frequency-centric. On the other hand, the cross-branch modules utilize multi-head attention to capture interactions not only between colors and densities but also among neighboring 3D points. This helps mitigate overfitting to high-frequency details by constraining color predictions through density-based, position-aware relationships. This also represents a *model-based* method that is compatible with INGP, which is highly sensitive to architectural changes.

4.2. Scene Decomposition with Discrete Wavelet loss

Given a pair of predicted view \mathbf{I} and ground-truth view \mathbf{I}_{gt} , the Discrete Wavelet (DW) loss minimizes the differences of their frequency representations:

$$\mathcal{L}_{DW} = \sum_{sb \in \{LL, LH, HL, HH\}} \lambda_{sb} \|\mathbf{I}^{sb} - \mathbf{I}_{gt}^{sb}\|_2^2$$

where λ_{sb} is the weighting for the corresponding sub-bands. By setting λ_{LL} higher than other sub-bands, we have explicitly prioritized learning of low frequencies. The DW loss is incorporated with the photometric loss \mathcal{L}_{MSE} , as well as all regularization losses used in CombiNeRF [2]:

$$\mathcal{L} = \mathcal{L}_{MSE} + \mathcal{L}_{DW} + \lambda_{dist} \mathcal{L}_{dist} + \lambda_{fg} \mathcal{L}_{fg} + \lambda_{ds} \mathcal{L}_{ds} + \lambda_{KL} \mathcal{L}_{KL}$$

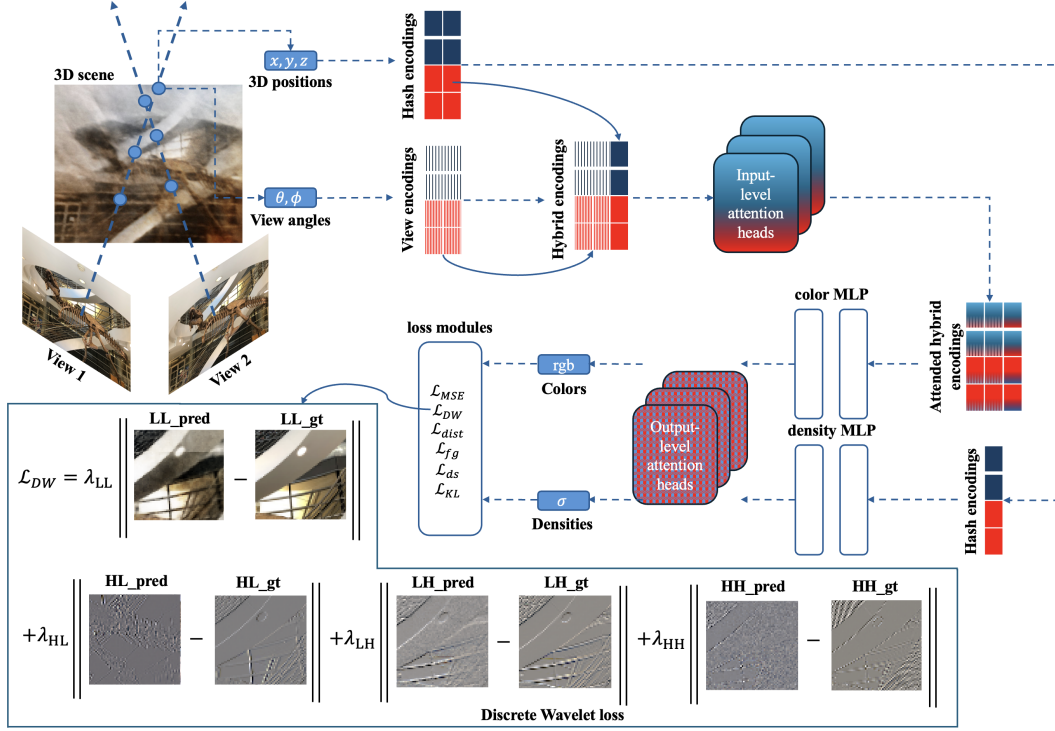


Figure 2. Architecture diagram of DWTNeRF. Firstly, we encode 3D positions with INGP’s [22] hash encoding, and the viewing directions with spherical harmonics [27]. Afterwards, we concatenate the view encodings with the hash encodings, to produce the “hybrid encodings”. We facilitate cross-branch interactions by feeding them into a multi-head attention [34] module. The attended hybrid encodings are inputs to the color MLP, while the hash encodings are inputs to the density MLP. Then, the MLP outputs from both branches are concatenated together, and again fed into another multi-head attention module. To supervise the quality of novel views, we use the usual photometric loss (\mathcal{L}_{MSE}) between the predicted and ground-truth views, as well as other regularization terms that are used in CombiNeRF [2].

where \mathcal{L}_{dist} is the distortion loss, introduced by Mip-NeRF 360 [1]. \mathcal{L}_{fg} is the full geometry loss, introduced by DiffusionNeRF [37]. \mathcal{L}_{ds} is the depth smoothness loss, introduced by RegNeRF [23]. \mathcal{L}_{KL} is the KL divergence loss, introduced by InfoNeRF [16]. The DW loss allows us to prioritize low frequencies directly in the training objective.

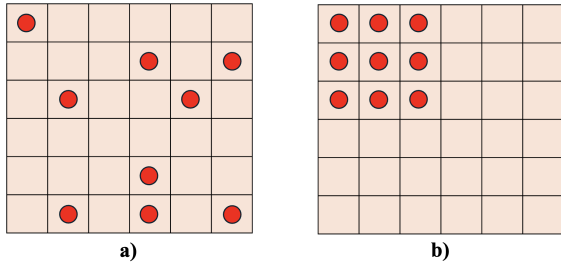


Figure 3. Random (left) and patch-based ray sampling (right). Patch sampling immediately forms a 2D image, and is compatible with the Discrete Wavelet Transform.

Patch-based Rendering The DW loss requires adjacently sampled rays \mathbf{r} that make up a 2D image \mathbf{I} . This requires patch-based ray sampling. As illustrated in Figure 3b, rays sampled in patches are adjacent to each other, making up a small square grid. Figure 3a shows rays sampled randomly throughout the image grid. We use random ray sampling for calculating \mathcal{L}_{MSE} , and patch-based for \mathcal{L}_{DW} . This design choice is intentional: it considers both global structures (random rays) and local structures (patch-based rays) in one iteration.

Lazy Regularization The sub-bands are 4 times smaller than the original image \mathbf{I} . For the DW loss to be feasible, however, the sub-bands still need to be visually meaningful. For example, \mathbf{I}^{LH} and \mathbf{I}^{HL} can highlight vertical and horizontal edges of a scene. By minimizing their differences with the ground-truths, we can better preserve those mid-frequency-level structures. This requires the rendered image \mathbf{I} to be large in the first place, or else its sub-bands would be too coarse. This incurs heavy computational overhead, because an N -sized square patch requires N^2 number of rays. We alleviate the problem as follows. Firstly, we follow

Algorithm 1 DWTNeRF Training Algorithm

Input: Dataset of observed views $\mathcal{D} = \{(\mathbf{I}_{full}, \mathbf{p})\}$, with pose \mathbf{p} for each full-resolution image \mathbf{I}_{full} ; current iteration t ; maximum iteration T ; randomly sampled batch size $|\mathcal{R}|$; patch-based sampled batch size $|\mathcal{R}_P|$; DW loss’s interval K_{DW} ; DW loss’s maximum iteration T_{DW} ; sub-band weights $\lambda_{(\cdot)}$; learning rate η_t

Output: Trained NeRF $f_{\theta}(\cdot, \cdot)$

Initialize NeRF $f_{\theta}(\cdot, \cdot)$

repeat

Randomly sample a ray batch \mathcal{R} , with corresponding ground-truth colors $\mathbf{c}_{gt}(\mathcal{R})$

Compute predicted colors $\mathbf{c}(\mathcal{R})$ by Equation (1)

$\mathcal{L} \leftarrow \mathcal{L}_{MSE}(\mathbf{c}(\mathcal{R}), \mathbf{c}_{gt}(\mathcal{R}))$

if $t \bmod K_{DW} = 0$ **and** $t < T_{DW}$ **then**

Sample a patch-based ray batch \mathcal{R}_P , with corresponding ground-truth colors $\mathbf{c}_{gt}(\mathcal{R}_P) \equiv \mathbf{I}_{gt}$

Compute predicted colors $\mathbf{c}(\mathcal{R}_P) \equiv \mathbf{I}$ by Equation (1)

Compute predicted sub-bands $\mathbf{I}^{LL}, \mathbf{I}^{LH}, \mathbf{I}^{HL}, \mathbf{I}^{HH}$

Compute ground-truth sub-bands $\mathbf{I}_{gt}^{LL}, \mathbf{I}_{gt}^{LH}, \mathbf{I}_{gt}^{HL}, \mathbf{I}_{gt}^{HH}$

$\mathcal{L} \leftarrow \mathcal{L} + \mathcal{L}_{DW}(\mathbf{I}^{(\cdot)}, \mathbf{I}_{gt}^{(\cdot)})$

end if

$\theta \leftarrow \text{Adam}(\theta, \eta_t, \nabla_{\theta} \mathcal{L})$

until $t > T$

the lazy regularization procedure inspired by [14], where we only calculates the DW loss every few iterations. Secondly, since we only prioritize low frequencies earlier in the training, we can safely stop calculating the DW loss later on. We present the full training algorithm of DWTNeRF at Algorithm 1. Here, we only detail \mathcal{L}_{MSE} and \mathcal{L}_{DW} for simplicity.

4.3. Cross-branch Interactions with Multi-head Attention

Our approach for cross-branch interactions consists of:

I. Cross-branch Concatenation We are given the hash encoding $\gamma_{0:N_x}(\mathbf{x})$ and the view encoding $\gamma_{0:N_d}(\mathbf{d})$. Here, the subscripts denote the dimension of the encoding. $0 : N_{(\cdot)}$ means the full dimension. N_x and N_d represent the highest dimensions of the hash and view encodings. The first stage involves concatenating the view encoding with all-but-the-first-dimension of the hash encoding. This can be written as $\gamma'(\mathbf{d}, \mathbf{x}) = [\gamma(\mathbf{d}), \gamma_{1:N_x}(\mathbf{x})]$, where $[\cdot, \cdot]$ denotes the concatenation operator. We call this the “hybrid encoding”. The hash encoding only retains its first dimension: $\gamma'(\mathbf{x}) = \gamma_0(\mathbf{x})$. The intuition is as follows. We will use $\gamma'(\mathbf{x})$ as inputs to the density MLP, and $\gamma'(\mathbf{d}, \mathbf{x})$ as inputs to the color MLP. Densities are irrespective of viewing directions and should only be position-dependent, so we make

$\gamma'(\mathbf{x})$ extremely lean to avoid over-parameterizing them. On the other hand, colors are both view- and position-dependent, which explains the concatenation.

II. Input-level Multi-head Attention We now have the “trimmed” hash encoding $\gamma'(\mathbf{x})$ and hybrid encoding $\gamma'(\mathbf{d}, \mathbf{x})$. We push $\gamma'(\mathbf{d}, \mathbf{x})$ into a multi-head attention module to learn the interactions between $\gamma(\mathbf{d})$ and $\gamma_{1:N_x}(\mathbf{x})$. Again, we leave $\gamma'(\mathbf{x})$ intact to not over-parameterize it. The multi-head attention is applied as: $\text{MultiHead}(\mathbf{Q}, \mathbf{K}, \mathbf{V}) = [\text{head}_0, \dots, \text{head}_H] \mathbf{W}^O$, where $\text{head}_i = \text{Attn}(\mathbf{Q} \mathbf{W}_i^Q, \mathbf{K} \mathbf{W}_i^K, \mathbf{V} \mathbf{W}_i^V)$. Here, Attn is simply the attention layer [34]. $\mathbf{Q}, \mathbf{K}, \mathbf{V}$ are the query, key and value matrices, all of which are set to $\gamma'(\mathbf{d}, \mathbf{x})$. $\mathbf{W}_i^Q, \mathbf{W}_i^K, \mathbf{W}_i^V$ are the corresponding learnable projection matrices. We note that $\gamma'(\mathbf{d}, \mathbf{x})$ is a tensor of size $|\mathcal{R}| \times (N_x - 1 + N_d)$. The choice of using attention is deliberate. Along the vertical dimension, it learns the interactions between all rays \mathbf{r} in the batch \mathcal{R} . This equates to learning the interactions between neighboring 3D points. Along the horizontal dimension, it learns the interactions between the positions and viewing directions. Using many heads, up to a maximum H , provides many of such interactions. The heads are concatenated, and then projected by another learnable matrix \mathbf{W}^O to ensure outputs and inputs are of the same size. We now write the attended hybrid encoding as $\gamma''(\mathbf{d}, \mathbf{x})$. The plenoptic function is now $f(\gamma'(\mathbf{x}), \gamma''(\mathbf{d}, \mathbf{x})) = \sigma, \mathbf{c}$, parameterized by two separate MLP branches for densities and colors.

III. Output-level Multi-head Attention f ’s outputs are the “preliminary” colors \mathbf{c} and densities σ . We again learn their interactions. We concatenate them together, and feed them into a multi-head attention module. Here, $\mathbf{Q}, \mathbf{K}, \mathbf{V}$ are set to $\zeta = [\sigma, \mathbf{c}]$. All intuitions in the second stage still hold. We “un-concatenate” the attended ζ' to obtain the final predictions. Specifically, the densities σ' are the first dimension of ζ' , and the colors \mathbf{c}' are the three remaining dimensions.

5. Experiments

5.1. Datasets & Implementation Details

Datasets & Metrics DWTNeRF is evaluated on the LLFF [20] dataset and the NeRF-Synthetic dataset [21], under few-shot conditions. Those are popular benchmarks for novel view synthesis. For the LLFF dataset, we evaluated the test metrics under 2/3/6/9 input views. For the NeRF-Synthetic (NS) dataset, we trained on 4 views and tested on 25 views. Those protocols are similar to previous works. We employed the PSNR, SSIM [35] and LPIPS [43] metrics to evaluate the quality of novel views.

Implementation Details DWTNeRF is built on top of CombiNeRF [2], which in turn is built on a Pytorch implementation of INGP, torch-ngp [31]. We kept all default

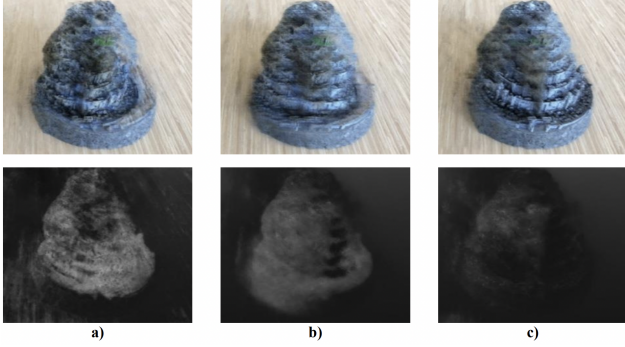


Figure 4. Qualitative results for Vanilla INGP (a), CombiNeRF (b) and DWTNeRF (c) on the LLFF [20] dataset (“fortress” scene). Top row depicts the novel views, while bottom row depicts the corresponding depth maps. Our DWTNeRF retains finer details better. The depth map generated by DWTNeRF is also more factual.

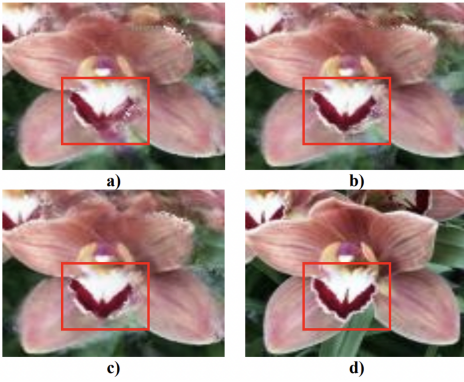


Figure 5. Qualitative results for CombiNeRF (a), DWTNeRF with no DW loss (b), DWTNeRF with both modules (c) and ground-truth (d) on the LLFF [20] dataset (“orchids” scene). Using the DW loss preserves structures better, which in turn produces the least pink-colored “hallucinations”, as depicted in the red region.

settings of CombiNeRF, and trained for 10K iterations in all experiments. We randomly sampled 4096 rays (for LLFF) and 7008 rays (for NS) in each iteration. For DW loss, we additionally sampled 36864 rays, leading to 192×192 square patches. We calculated the DW loss every 10 (for LLFF) and 150 (for NS) iterations, but stopped altogether at 5K iterations to facilitate high-frequency learning. For LLFF, we set the LL sub-band weight as 0.4, the other sub-bands were 0.2. For NS, LL sub-band weight was 0.04, the rest were all 0.02. This ensures that the low frequencies were the most important. Finally, we used 2 (for LLFF) and 1 (for NS) attention heads for both input and output levels. All trainings were done with GeForce RTX 4070 Ti Super.

5.2. Qualitative Results

Figure 4 shows the qualitative results between Vanilla INGP, CombiNeRF and our DWTNeRF. The chosen scene is “fortress”. Our DWTNeRF clearly better retains the fine structures of the fortress. As for depth maps, both CombiNeRF and DWTNeRF dramatically lessen floating artifacts that are extremely prevalent in Vanilla INGP. DWTNeRF’s depth map is also more factual than CombiNeRF: the fortress should generally be as far to the camera as the table.

Figure 5 shows a more ablation-level analysis that demonstrates the effects of using the DW loss. The chosen scene is “orchids”. With the DW loss, we additionally gain a supervision on the low- and middle frequencies. This translates to better preserved structures, and less 3D “hallucinations”. We provide more qualitative results of both LLFF and NeRF-Synthetic at Section 7 of Appendix.

5.3. Quantitative Results

On LLFF We compared DWTNeRF against recent few-shot works published at top venues. Regularization methods include InfoNeRF [16], FreeNeRF [39] and CombiNeRF [2]. Prior methods include DietNeRF [11], RegNeRF [23], DiffusioNeRF [37] and GeCoNeRF [17]. Model method includes mi-MLP [46]. Table 1 shows the quantitative results. Methods with the symbol \dagger were reproduced on our machine, keeping all default settings. Unavailable metrics are denoted “—”. The best-performing metrics under each few-shot condition are **bolded**. In the 2-shot case, DWTNeRF outperforms CombiNeRF by 1.6% in PSNR, 0.84% in SSIM and 4.17% in LPIPS. The effects of our DWTNeRF are still strongly seen with 3-shot, but generally fade with higher views, suggesting its high compatibility with extreme few-shot conditions.

On NeRF-Synthetic Table 2 shows the quantitative results. In the 4-shot case, DWTNeRF outperforms CombiNeRF by 0.5% in PSNR, 0.1% in SSIM and 0.9% in LPIPS.

5.4. Ablation Studies

In this section, we validated the design choices of DWTNeRF. Ablations were done on the 3-shot LLFF benchmark.

On main modules Those are the DW loss and the cross-branch interactions. Table 3 shows the effects of each module. The second row removes the frequency masking from CombiNeRF, given its incompatibility with INGP. This provides improvements in all metrics. The third row is our DWTNeRF, but with the DW loss only. Starting from the fourth row, we examine the effects of using multi-head attention in cross-branch interactions. The fourth row is DWTNeRF with only input-level attention. The fifth row only has output-level attention. The sixth row combines both levels. This produces stronger results over the previous two. The final row combines both DW loss and cross-branch interactions, which provides the strongest results.

Table 1. Comparison of DWTNeRF against SOTA methods under 2/3/6/9 views, LLFF dataset [20]

METHOD	VENUE	PSNR (\uparrow)				SSIM (\uparrow)				LPIPS (\downarrow)			
		2-VIEW	3-VIEW	6-VIEW	9-VIEW	2-VIEW	3-VIEW	6-VIEW	9-VIEW	2-VIEW	3-VIEW	6-VIEW	9-VIEW
VANILLA INGP	ARXIV '22	16.59	17.71	22.03	24.21	0.458	0.544	0.738	0.811	0.359	0.303	0.149	0.101
GECONeRF	ICML '23	-	18.77	-	-	-	0.596	-	-	-	0.338	-	-
FREENeRF	CVPR '23	-	19.63	23.73	25.13	-	0.612	0.779	0.827	-	0.308	0.195	0.160
DIFFUSIONeRF	CVPR '23	-	19.79	23.79	25.02	-	0.568	0.747	0.785	-	0.338	0.237	0.212
MI-MLP	CVPR '24	-	19.75	23.57	25.15	-	0.614	0.788	0.834	-	0.300	0.163	0.140
COMBiNeRF \dagger	3DV '24	16.47	20.12	24.05	25.24	0.475	0.676	0.801	0.836	0.336	0.197	0.105	0.084
DWTNeRF (OURS)	-	16.73	20.38	24.04	25.20	0.479	0.677	0.801	0.835	0.322	0.193	0.104	0.084

Table 2. Comparison of DWTNeRF against SOTA methods under 4 views, NeRF-Synthetic dataset [21]

METHOD	VENUE	PSNR (\uparrow)	SSIM (\uparrow)	LPIPS (\downarrow)
DIETNeRF	ICCV '21	15.42	0.730	0.314
VANILLA INGP \dagger	ARXIV '22	17.49	0.734	0.357
REGNeRF	CVPR '22	13.71	0.786	0.346
INFONeRF	CVPR '22	18.44	0.792	0.223
COMBiNeRF \dagger	3DV '24	19.15	0.792	0.224
DWTNeRF (OURS)	-	19.25	0.793	0.222

Table 3. Ablation on DWTNeRF’s main modules, LLFF dataset [20]

METHOD	PSNR (\uparrow)	SSIM (\uparrow)	LPIPS (\downarrow)
COMBiNeRF (BASELINE) \dagger	20.12	0.676	0.197
COMBiNeRF (-FREQ. MASK.) \dagger	20.19	0.677	0.194
DWTNeRF (+DW.)	20.25	0.677	0.193
DWTNeRF (+INP. ATTN.)	20.33	0.670	0.195
DWTNeRF (+OUTP. ATTN.)	20.34	0.670	0.195
DWTNeRF (+FULL CB.)	20.36	0.670	0.195
DWTNeRF (+BOTH)	20.38	0.677	0.193

Table 4. Comparison against prior and model methods, LLFF dataset [20]

METHOD	TYPE	PSNR (\uparrow)	SSIM (\uparrow)	LPIPS (\downarrow)
COMBiNeRF (BASELINE) \dagger	R	20.12	0.676	0.197
DIETNeRF (+FULL CB.) \dagger	M, P	20.29	0.671	0.194
SPARF (+FULL CB.) \dagger	M, P	19.28	0.618	0.261
DWTNeRF (+FULL CB. + DW.)	M, R	20.38	0.677	0.193
COMBiNeRF (BASELINE) \dagger	R	20.12	0.676	0.197
COMBiNeRF (+RES.) \dagger	M, R	20.20	0.664	0.198
COMBiNeRF (+RES.+) \dagger	M, R	19.99	0.650	0.204
COMBiNeRF (+ELE. CB.) \dagger	M, R	19.90	0.667	0.205
DWTNeRF (+FULL CB.)	M, R	20.36	0.670	0.195

On prior methods We implemented two prior-based approaches on top of CombiNeRF: DietNeRF’s semantic consistency (SC) loss [11] and SPARF’s multi-view (MV) correspondence loss [33]. We simply replaced the DW loss at Algorithm 1 with these losses. Table 4 (upper half) shows the results. “R”, “P”, “M” stand for regularization-, prior-

and model-based, respectively. Our DW loss outperforms SC loss, but the DWT is much more lightweight than computing feature embeddings from a CLIP model. This suggests frequency supervision can be as important as semantic supervision. Performance worsens with MV loss, suggesting the multi-view correspondences are not a useful prior for INGP. For more implementation details, please refer to Sections 9 and 10 of Appendix.

On model methods We implemented two model-based approaches on top of CombiNeRF: “Residual Connections” (Figure 6a) and “Element-wise Cross-branch Interactions” (Figure 6b) - both introduced by mi-MLP [46]. Table 4 (lower half) shows the results. The second row introduces residuals. The third row is the same, but we added one MLP layer, hoping to better highlight the residuals’ effects. However, this degraded performances noticeably, highlighting the vulnerability of INGP to architectural changes. The fourth row shows mi-MLP’s cross-branch interactions. Only our version of interactions is competitive with the baseline. For more implementation details, please refer to Section 13 of Appendix.

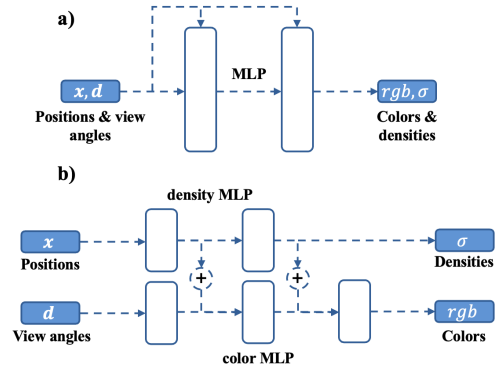


Figure 6. mi-MLP’s [46] model methods: “Residual Connections” (a) and “Element-wise Cross-branch Interactions” (b)

On the choice of wavelets We compared the effects of different Daubechies wavelets [6] on the DW loss. We started

Table 5. Ablation on wavelets for DW loss

METHOD	PSNR (\uparrow)	SSIM (\uparrow)	LPIPS (\downarrow)
COMBINeRF (BASELINE) \dagger	20.12	0.676	0.197
DWTNeRF (+DW. / HAAR)	20.25	0.677	0.193
DWTNeRF (+DW. / DB2)	20.23	0.678	0.193
DWTNeRF (+DW. / DB3)	20.23	0.678	0.192

with the Haar ($n = 1$) and then higher-order wavelets, up to the db3 ($n = 3$). Generally, higher-order wavelets have more supports, and spreads the signal energy more evenly across sub-bands. Section 8 of Appendix shows the exact wavelet coefficients. Figure 7 compares scene decomposition using the Haar versus db2 ($n = 2$). Compared to the ground-truths, the rendered sub-bands are much noisier, highlighting the purpose of the DW loss. The db2 provides finer details. However, table 5 shows no significant differences between the wavelets. This confirms our intuition that low-frequency supervision is sufficient.

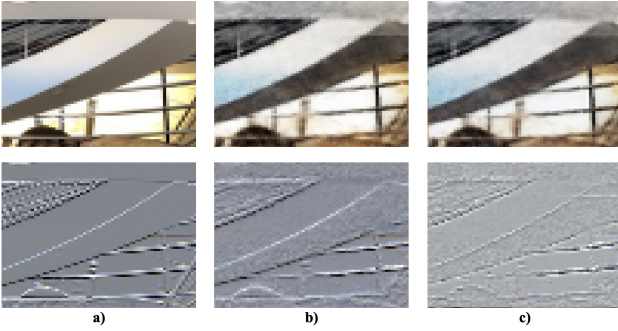


Figure 7. Decomposition using the Haar (a & b) and db2 (c). We only show the LL (top) and LH (bottom) sub-bands. Column a) is the ground-truth LL, much less noisier than rendered LL at column b). Column c) uses higher-order wavelet, and shows finer details.

6. Conclusion

INGP-based models have distinct characteristics that might make them incompatible with recent few-shot approaches. Firstly, they are fast-converging, and vulnerable to architectural changes under few-shot conditions. This requires a re-thinking in *model-based* approaches. For this, we introduce a cross-branch interaction pipeline based on multi-head attention, which acts on NeRF’s inputs & outputs, but not on the MLP layers. Secondly, based on multi-resolution, INGP does not explicitly map the inputs into a range of frequencies. This requires a re-thinking in *frequency-* and *regularization-based* approaches. For this, we introduce a novel Discrete Wavelet loss that decomposes the scenes into

different frequencies and allows explicit prioritization of low frequencies in earlier training stages.

Limitations & Future Works Firstly, the DWT does not disentangle high-frequency components. For example, besides fine structural details, high frequencies can come from specularities and other light-dependent effects. Future works might explore scene decomposition at such further levels. Secondly, since the DW loss is used as an auxiliary loss alongside the photometric MSE loss, which compares pixel-wise differences regardless of frequencies, we believe some high-frequency overfitting still exists. Our DW loss *prioritizes* low frequencies, but not *eliminate* high frequencies in early training. Future works could tackle this problem, but interfering with the photometric loss can be tricky. We can also investigate the applicability of our methods to other representations, like SDF [3, 18] or 3DGS [15].

References

- [1] Jonathan T. Barron, Ben Mildenhall, Dor Verbin, Pratul P. Srinivasan, and Peter Hedman. Mip-nerf 360: Unbounded anti-aliased neural radiance fields. In *2022 IEEE/CVF Conference on Computer Vision and Pattern Recognition (CVPR)*, pages 5460–5469, 2022. 2, 4
- [2] Matteo Bonotto, Luigi Sarrocco, Daniele Evangelista, Marco Imperoli, and Alberto Pretto. CombiNeRF: A Combination of Regularization Techniques for Few-Shot Neural Radiance Field View Synthesis. In *International Conference on 3D Vision (3DV)*, 2024. 2, 3, 4, 5, 6
- [3] T. Chan and Wei Zhu. Level set based shape prior segmentation. In *2005 IEEE Computer Society Conference on Computer Vision and Pattern Recognition (CVPR’05)*, pages 1164–1170 vol. 2, 2005. 8
- [4] Zixuan Chen, Lingxiao Yang, Jian-Huang Lai, and Xiaohua Xie. Cunerf: Cube-based neural radiance field for zero-shot medical image arbitrary-scale super resolution. In *2023 IEEE/CVF International Conference on Computer Vision (ICCV)*, pages 21128–21138, 2023. 1
- [5] Abril Corona-Figueroa, Jonathan Frawley, Sam Bond Taylor, Sarath Bethapudi, Hubert P. H. Shum, and Chris G. Willcocks. Mednerf: Medical neural radiance fields for reconstructing 3d-aware ct-projections from a single x-ray. In *2022 44th Annual International Conference of the IEEE Engineering in Medicine & Biology Society (EMBC)*, pages 3843–3848, 2022. 1
- [6] Ingrid Daubechies. *Ten Lectures on Wavelets*. Society for Industrial and Applied Mathematics, 1992. 7, 1
- [7] Kyle Gao, Yina Gao, Hongjie He, Dening Lu, Linlin Xu, and Jonathan Li. Nerf: Neural radiance field in 3d vision, a comprehensive review, 2023. 2
- [8] Guangcong, Zhaoxi Chen, Chen Change Loy, and Ziwei Liu. Sparsenerf: Distilling depth ranking for few-shot novel view synthesis. *IEEE/CVF International Conference on Computer Vision (ICCV)*, 2023. 2
- [9] Kaiming He, Xiangyu Zhang, Shaoqing Ren, and Jian Sun. Deep residual learning for image recognition. In *2016 IEEE*

- Conference on Computer Vision and Pattern Recognition (CVPR)*, pages 770–778, 2016. 2
- [10] Gao Huang, Zhuang Liu, Laurens Van Der Maaten, and Kilian Q. Weinberger. Densely connected convolutional networks. In *2017 IEEE Conference on Computer Vision and Pattern Recognition (CVPR)*, pages 2261–2269, 2017. 2
- [11] Ajay Jain, Matthew Tancik, and Pieter Abbeel. Putting nerf on a diet: Semantically consistent few-shot view synthesis. In *Proceedings of the IEEE/CVF International Conference on Computer Vision (ICCV)*, pages 5885–5894, 2021. 2, 6, 7, 1, 3
- [12] Kyungmin Jo, Gyumin Shim, Sanghun Jung, Soyoung Yang, and Jaegul Choo. Cg-nerf: Conditional generative neural radiance fields for 3d-aware image synthesis. In *2023 IEEE/CVF Winter Conference on Applications of Computer Vision (WACV)*, pages 724–733, 2023. 2
- [13] James T. Kajiya and Brian Von Herzen. Ray tracing volume densities. *Proceedings of the 11th annual conference on Computer graphics and interactive techniques*, 1984. 3
- [14] Tero Karras, Samuli Laine, Miika Aittala, Janne Hellsten, Jaakko Lehtinen, and Timo Aila. Analyzing and improving the image quality of stylegan. In *2020 IEEE/CVF Conference on Computer Vision and Pattern Recognition (CVPR)*, pages 8107–8116, 2020. 5
- [15] Bernhard Kerbl, Georgios Kopanas, Thomas Leimkühler, and George Drettakis. 3d gaussian splatting for real-time radiance field rendering. *ACM Transactions on Graphics*, 42(4), 2023. 8, 3
- [16] Mijeong Kim, Seonguk Seo, and Bohyung Han. Infonerf: Ray entropy minimization for few-shot neural volume rendering. In *2022 IEEE/CVF Conference on Computer Vision and Pattern Recognition (CVPR)*, pages 12902–12911, 2022. 2, 4, 6
- [17] Minseop Kwak, Jiuhn Song, and Seungryong Kim. Geconerf: Few-shot neural radiance fields via geometric consistency. *arXiv preprint arXiv:2301.10941*, 2023. 2, 6, 3
- [18] Runfa Blark Li, Keito Suzuki, Bang Du, Ki Myung Brian Le, Nikolay Atanasov, and Truong Nguyen. Splat sdf: Boosting neural implicit sdf via gaussian splatting fusion, 2024. 8
- [19] Carl Lindström, Georg Hess, Adam Lilja, Maryam Fatemi, Lars Hammarstrand, Christoffer Petersson, and Lennart Svensson. Are nerfs ready for autonomous driving? towards closing the real-to-simulation gap. In *2024 IEEE/CVF Conference on Computer Vision and Pattern Recognition Workshops (CVPRW)*, pages 4461–4471, 2024. 1
- [20] Ben Mildenhall, Pratul P. Srinivasan, Rodrigo Ortiz-Cayon, Nima Khademi Kalantari, Ravi Ramamoorthi, Ren Ng, and Abhishek Kar. Local light field fusion: Practical view synthesis with prescriptive sampling guidelines. *ACM Transactions on Graphics (TOG)*, 2019. 5, 6, 7
- [21] Ben Mildenhall, Pratul P. Srinivasan, Matthew Tancik, Jonathan T. Barron, Ravi Ramamoorthi, and Ren Ng. Nerf: Representing scenes as neural radiance fields for view synthesis. In *ECCV*, 2020. 1, 2, 5, 7, 6
- [22] Thomas Müller, Alex Evans, Christoph Schied, and Alexander Keller. Instant neural graphics primitives with a multiresolution hash encoding. *ACM Trans. Graph.*, 41(4):102:1–102:15, 2022. 1, 2, 4
- [23] Michael Niemeyer, Jonathan T. Barron, Ben Mildenhall, Mehdi S. M. Sajjadi, Andreas Geiger, and Noha Radwan. Regnerf: Regularizing neural radiance fields for view synthesis from sparse inputs. In *2022 IEEE/CVF Conference on Computer Vision and Pattern Recognition (CVPR)*, pages 5470–5480, 2022. 2, 4, 6
- [24] Matt Pharr, Wenzel Jakob, and Greg Humphreys. *Physically Based Rendering: From Theory to Implementation*. Morgan Kaufmann Publishers Inc., San Francisco, CA, USA, 3rd edition, 2016. 3
- [25] Albert Pumarola, Enric Corona, Gerard Pons-Moll, and Francesc Moreno-Noguer. D-NeRF: Neural Radiance Fields for Dynamic Scenes. In *Proceedings of the IEEE/CVF Conference on Computer Vision and Pattern Recognition*, 2020. 2
- [26] Nasim Rahaman, Aristide Baratin, Devansh Arpit, Felix Draxler, Min Lin, Fred A. Hamprecht, Yoshua Bengio, and Aaron C. Courville. On the spectral bias of neural networks. In *ICML*, pages 5301–5310. PMLR, 2019. 1
- [27] Ravi Ramamoorthi. Modeling illumination variation with spherical harmonics. 2005. 4
- [28] Sara Fridovich-Keil and Alex Yu, Matthew Tancik, Qinhong Chen, Benjamin Recht, and Angjoo Kanazawa. Plenoxels: Radiance fields without neural networks. In *CVPR*, 2022. 1
- [29] Seunghyeon Seo, Yeonjin Chang, and Nojun Kwak. Flipnerf: Flipped reflection rays for few-shot novel view synthesis. In *2023 IEEE/CVF International Conference on Computer Vision (ICCV)*, pages 22826–22836, 2023. 1
- [30] Gilbert Strang and Truong Nguyen. *Wavelets and filter banks*. SIAM, 1996. 3, 1
- [31] Jiaxiang Tang. Torch-ngp: a pytorch implementation of instant-ngp, 2022. <https://github.com/ashawkey/torch-ngp>. 5
- [32] Adam Tonderski, Carl Lindström, Georg Hess, William Ljungbergh, Lennart Svensson, and Christoffer Petersson. Neurad: Neural rendering for autonomous driving. In *Proceedings of the IEEE/CVF Conference on Computer Vision and Pattern Recognition*, pages 14895–14904, 2024. 1
- [33] Prune Truong, Marie-Julie Rakotosaona, Fabian Manhardt, and Federico Tombari. Sparf: Neural radiance fields from sparse and noisy poses. *IEEE/CVF Conference on Computer Vision and Pattern Recognition, CVPR*, 2023. 2, 7, 1, 3
- [34] Ashish Vaswani, Noam Shazeer, Niki Parmar, Jakob Uszkoreit, Llion Jones, Aidan N Gomez, Łukasz Kaiser, and Illia Polosukhin. Attention is all you need. In *Advances in neural information processing systems*, pages 5998–6008, 2017. 4, 5
- [35] Zhou Wang, A.C. Bovik, H.R. Sheikh, and E.P. Simoncelli. Image quality assessment: from error visibility to structural similarity. *IEEE Transactions on Image Processing*, 13(4): 600–612, 2004. 5
- [36] Chung-Yi Weng, Brian Curless, Pratul P. Srinivasan, Jonathan T. Barron, and Ira Kemelmacher-Shlizerman. HumanNeRF: Free-viewpoint rendering of moving people from monocular video. In *Proceedings of the IEEE/CVF Conference on Computer Vision and Pattern Recognition (CVPR)*, pages 16210–16220, 2022. 1
- [37] Jamie Wynn and Daniyar Turmukhambetov. Diffusionerf: Regularizing neural radiance fields with denoising diffusion

- models. In *2023 IEEE/CVF Conference on Computer Vision and Pattern Recognition (CVPR)*, pages 4180–4189, 2023. [2](#), [4](#), [6](#)
- [38] Linning Xu, Vasu Agrawal, William Laney, Tony Garcia, Aayush Bansal, Changil Kim, Samuel Rota Bulò, Lorenzo Porzi, Peter Kotschieder, Aljaž Božič, Dahua Lin, Michael Zollhöfer, and Christian Richardt. VR-NeRF: High-fidelity virtualized walkable spaces. In *SIGGRAPH Asia Conference Proceedings*, 2023. [1](#)
 - [39] Jiawei Yang, Marco Pavone, and Yue Wang. Freenerf: Improving few-shot neural rendering with free frequency regularization. In *Proc. IEEE Conf. on Computer Vision and Pattern Recognition (CVPR)*, 2023. [1](#), [2](#), [6](#)
 - [40] Jianglong Ye, Naiyan Wang, and Xiaolong Wang. Featurenerf: Learning generalizable nerfs by distilling foundation models. In *Proceedings of the IEEE/CVF International Conference on Computer Vision*, pages 8962–8973, 2023. [2](#)
 - [41] Alex Yu, Ruilong Li, Matthew Tancik, Hao Li, Ren Ng, and Angjoo Kanazawa. PlenOctrees for real-time rendering of neural radiance fields. In *ICCV*, 2021. [2](#)
 - [42] Alex Yu, Vickie Ye, Matthew Tancik, and Angjoo Kanazawa. pixelNeRF: Neural radiance fields from one or few images. In *CVPR*, 2021. [2](#)
 - [43] Richard Zhang, Phillip Isola, Alexei A Efros, Eli Shechtman, and Oliver Wang. The unreasonable effectiveness of deep features as a perceptual metric. In *CVPR*, 2018. [5](#)
 - [44] Allan Zhou, Moo Jin Kim, Lirui Wang, Pete Florence, and Chelsea Finn. Nerf in the palm of your hand: Corrective augmentation for robotics via novel-view synthesis. In *2023 IEEE/CVF Conference on Computer Vision and Pattern Recognition (CVPR)*, pages 17907–17917, 2023. [1](#)
 - [45] Haidong Zhu, Yuyin Sun, Chi Liu, Lu Xia, Jiajia Luo, Nan Qiao, Ram Nevatia, and Cheng-Hao Kuo. Multimodal neural radiance field. In *2023 IEEE International Conference on Robotics and Automation (ICRA)*, pages 9393–9399, 2023. [1](#)
 - [46] Hanxin Zhu, Tianyu He, Xin Li, Bingchen Li, and Zhibo Chen. Is vanilla mlp in neural radiance field enough for few-shot view synthesis? In *Proceedings of the IEEE/CVF Conference on Computer Vision and Pattern Recognition (CVPR)*, pages 20288–20298, 2024. [1](#), [2](#), [6](#), [7](#), [4](#)

DWTNeRF: Boosting Few-shot Neural Radiance Fields via Discrete Wavelet Transform

Supplementary Material

7. More Visualizations

We provide more qualitative results on the 3-shot LLFF and 4-shot NeRF-Synthetic benchmarks at Figures 13 and 12. There are 6 scenes in total. In each scene, we would like to direct attention towards the regions enclosed by the **red** box, which highlights the effects of cross-branch interactions ($b \rightarrow c$) and DW loss ($c \rightarrow d$). They provide finer details, preserve better structures and reduce random “hallucinated” points in 3D space.

8. Wavelet Coefficients

Table 6. Low-pass filters of the Daubechies [6] wavelets

ORDER	1	2	3
ℓ_k	1	$1 + \sqrt{3}$	0.3327
	1	$3 + \sqrt{3}$	0.8069
		$3 - \sqrt{3}$	0.4599
		$1 - \sqrt{3}$	-0.1350
			-0.0854
			0.0352
FACTOR	$\sqrt{2}$	$4\sqrt{2}$	1

Table 6 shows the coefficients ℓ_k of the 1D low-pass filters ℓ that are used in our experiments. The corresponding 2D low-pass matrices \mathbf{L} are constructed with shifting rows of ℓ :

$$\mathbf{L} = \begin{pmatrix} \cdots & \cdots & \cdots & & & & \\ \cdots & \ell_{-1} & \ell_0 & \ell_1 & \cdots & & \\ & & \cdots & \ell_{-1} & \ell_0 & \ell_1 & \cdots \\ & & & & \cdots & \cdots & \end{pmatrix}$$

and similarly for how \mathbf{H} is constructed with the 1D high-pass filter \mathbf{h} . We experimented with orthogonal Daubechies wavelets [30], where \mathbf{h} is derived trivially from ℓ according to the “Alternating Flip” condition:

$$h_k = (-1)^k \ell_{N-1-k}$$

where k denotes a single index of the 1D filter with number of coefficients N . As a numerical example, suppose that $\ell = [\ell_0, \ell_1, \ell_2, \ell_3]$, the corresponding \mathbf{h} that meets “Alternating Flip” condition is $\mathbf{h} = [\ell_3, -\ell_2, \ell_1, -\ell_0]$. In summary, while the DW loss can technically be classified as a prior

method, we classify it as a regularization method as it needs no more priors than the 1D low-pass filter ℓ . Besides its simplicity, the DW loss outperforms methods based on pre-trained weights like DietNeRF’s [11] semantic consistency loss and SPARF’s [33] multi-view correspondence loss - two highly popular representatives of prior methods. We discuss those methods in the next two sections.

We also provide more visualizations of scene decompositions using different wavelets in Figure 8. Higher-order wavelets spread energy more evenly across sub-bands, resulting in more fine-grained details. However, as presented in Table 5, this is not strictly necessary, confirming our intuition that low-frequency supervision is sufficient. While technically the db3 is best-performing, it is costlier due to having more coefficients. Therefore, the Haar was our method of choice.

9. Frequency vs. semantic supervision

The semantic consistency (SC) loss [11] minimizes discrepancies in embeddings of rendered and ground-truth views:

$$\mathcal{L}_{SC} = \frac{\lambda_{SC}}{2} \|\phi[\mathbf{I}_{gt}(\mathbf{p})] - \phi[\mathbf{I}(\hat{\mathbf{p}})]\|_2^2$$

where $\phi[\cdot]$ represents the image embeddings. $\mathbf{I}(\hat{\mathbf{p}})$ and $\mathbf{I}_{gt}(\mathbf{p})$ are the rendered and ground-truth views sampled from an interpolated *novel* view $\hat{\mathbf{p}}$ and nearest *known* view \mathbf{p} , respectively. The intuition is that, an object is what it is, regardless of the viewing direction. This is the core principle of the semantic supervision, which encourages high-level semantic information to be consistent across views.

In practice, DietNeRF uses the CLIP [?] embeddings, which are normalized. Since $\phi[\cdot]$ is a unit vector, the semantic loss reduces to a cosine similarity weighted by the balancing term λ_{SC} :

$$\mathcal{L}_{SC} = \lambda_{SC} \phi[\mathbf{I}_{gt}(\mathbf{p})]^T \phi[\mathbf{I}(\hat{\mathbf{p}})]$$

Implementation Details To compare the DW and SC losses fairly, we simply replaced the DW loss with the SC loss in Algorithm 1, and kept all other hyperparameters intact, except that the weight λ_{SC} was set to 0.01 and the interval K_{SC} was set to 30. Note that $K_{SC} > K_{DW} = 10$ to make the training feasible, as calculating CLIP embeddings is computationally intensive. Similar to DietNeRF, to

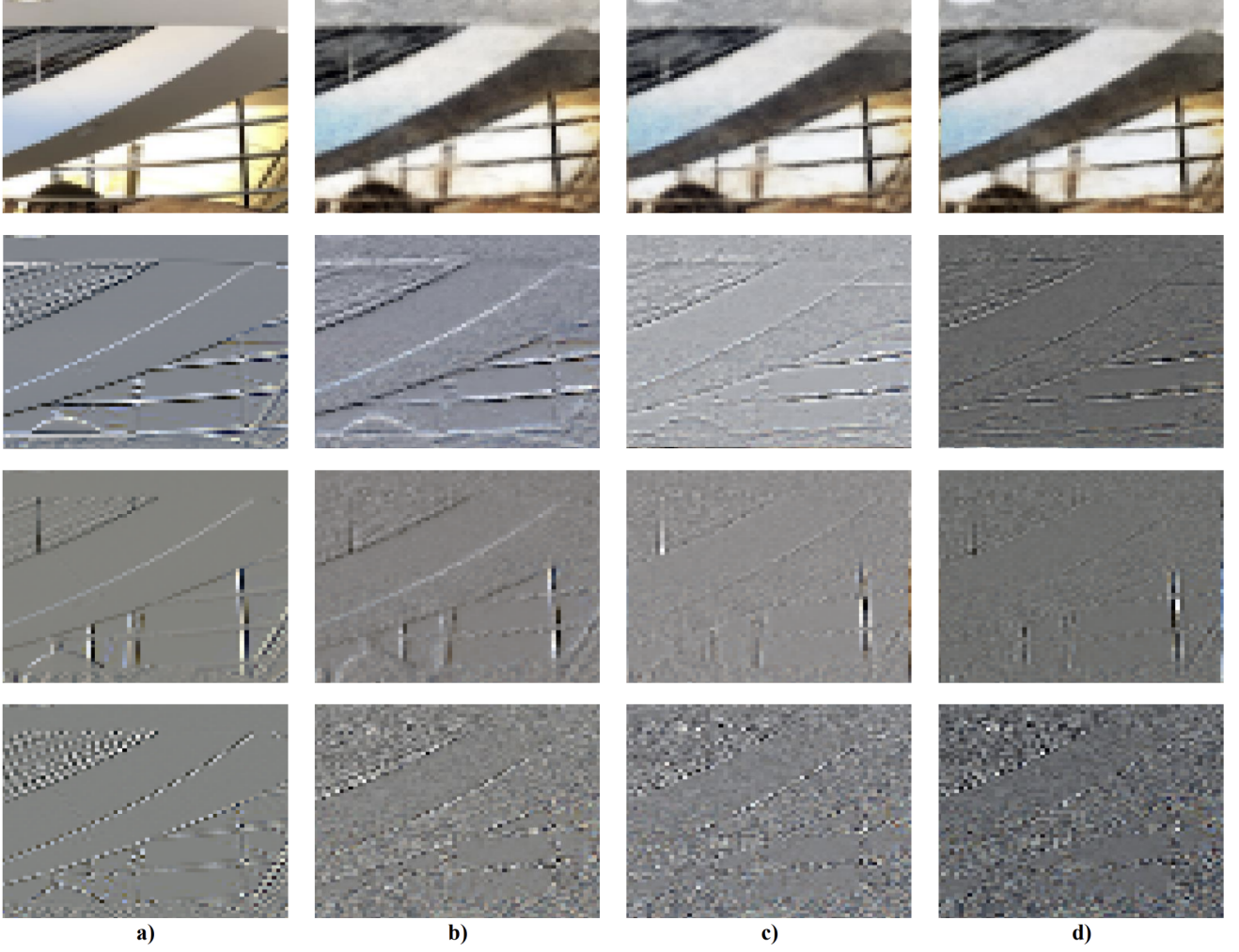


Figure 8. Frequency-based scene decompositions with different wavelets. From top to bottom: the LL, LH, HL and HH sub-bands. The first column (a) shows the sub-bands of ground-truth views using the Haar. The second column (b) is the same, but for rendered views, which are much noisier. The rest show sub-bands of rendered views using the db2 (c) and db3 (d). Higher-order wavelets provide more fine-grained details, but our experiments showed low-frequency supervision with coarse details is sufficient.

calculate the SC loss, we downsampled the known views to only 20% of the original resolution, and sampled rays across the downsampled image grid (so unlike DW loss, there was no use of patch-based rendering). The downsampling allows the rendering of novel views $\mathbf{I}(\hat{\mathbf{p}})$ to be computationally feasible. Furthermore, to sample a novel pose $\hat{\mathbf{p}}$, we sampled a pair of known views $\{\mathbf{p}_i, \mathbf{p}_j\}$, and a weighting factor $\alpha \sim \mathcal{U}(0, 1)$. Then, $\hat{\mathbf{p}} = \alpha \mathbf{p}_i + (1 - \alpha) \mathbf{p}_j$. If $\alpha > 0.5$, then \mathbf{p}_i is the ground-truth pose and vice versa.

As presented in Table 4, the DW loss outperforms the SC loss with a comfortable margin, but requires no use of pre-trained weights. Given that semantic supervision is a popular method (e.g. in DietNeRF [11], GeCoNeRF [17], CaesarNeRF [?]), we hope our results encourage fellow

researchers to explore frequency supervision, a new kind of supervision that might be equally effective but absolutely less computationally demanding.

10. Frequency vs. multi-view supervision

We additionally considered the multi-view supervision, utilized by the works of SPARF [33], CorresNeRF [?], ConsistentNeRF [?], GeCoNeRF [17], SGCNeRF [?], P²NeRF [?], etc. For comparison, we implemented SPARF’s multi-view (MV) correspondence loss, which minimizes errors of pixel matches’ projections between known views:

$$\mathcal{L}_{MV} = \lambda_{MV} \mathbf{w}_{\mathbf{p}_i, \mathbf{p}_j} f_{huber}[\mathbf{x}(\mathbf{p}_j) - \mathbf{x}_{gt}(\mathbf{p}_j)]$$

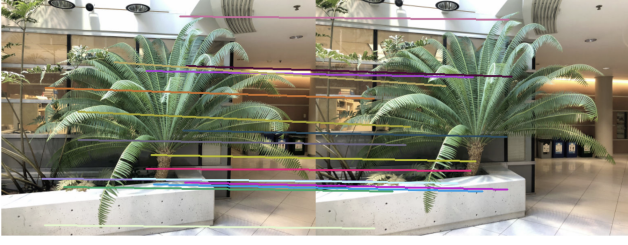


Figure 9. Pixel matches predicted by a trained OmniGlue [?], filtered by confidences (“fern” scene). There are a few incorrect matches, possibly reducing the effects of correspondence methods.

where \mathbf{p}_i and \mathbf{p}_j represent two known poses. A trained feature matching model predicts the pixel matches between the two, $\{\mathbf{x}_{gt}(\mathbf{p}_i), \mathbf{x}_{gt}(\mathbf{p}_j)\}$. We project the known matches in pose \mathbf{p}_i to the 3D space, and then back onto another view at the pose \mathbf{p}_j . This gives the predicted matches $\mathbf{x}(\mathbf{p}_j)$, which should be the same as $\mathbf{x}_{gt}(\mathbf{p}_j)$ for a perfectly geometrically correct solution [?]. This is the multi-view correspondence principle. This loss constrains the implicit 3D model to be geometrically accurate. f_{huber} is the Huber loss function [?], weighted by the matches confidences $\mathbf{w}_{\mathbf{p}_i, \mathbf{p}_j}$ and the balancing term λ_{MV} .

Attempting to re-produce the best version of the MV loss, we supplemented it with ideas from follow-up works of SPARF. Firstly, we implemented CorresNeRF’s matches augmentation strategy [?], which swaps the target and query images to produce more matches. This is in line with SPARF’s observation that the training benefits from an increasing number of *correct* matches. Secondly, also inspired by CorresNeRF, we implemented what we call the “two-way” MV loss:

$$\mathcal{L}_{MV} = \lambda_{MV} \mathbf{w}_{\mathbf{p}_i, \mathbf{p}_j} \frac{\sum_{n \in \{i, j\}} f_{huber}[\mathbf{x}(\mathbf{p}_n) - \mathbf{x}_{gt}(\mathbf{p}_n)]}{2}$$

Compared to the Vanilla MV loss, the two-way MV loss additionally starts with known matches in pose \mathbf{p}_j . They are similarly projected to 3D, and back-projected onto the view at pose \mathbf{p}_i . This provides predicted matches $\mathbf{x}(\mathbf{p}_i)$, then compared with ground-truths $\mathbf{x}_{gt}(\mathbf{p}_i)$. Intuitively, the two-way MV loss can provide more rigid geometric supervisions, as in one iteration both directions are considered.

Implementation Details Again, to compare the DW and MV losses fairly, we simply replaced the DW loss with the MV loss in Algorithm 1, and kept other hyperparameters intact, except that the weight λ_{MV} was set to 0.001. In each iteration, we sampled a pair of known views $\{\mathbf{p}_i, \mathbf{p}_j\}$, and calculated the MV loss. We used a trained OmniGlue [?] for predicting matches with good generalization. To better ensure matches quality, we filtered out correspondences with

confidences $\mathbf{w}_{\mathbf{p}_i, \mathbf{p}_j} < 0.5$. Figure 9 presents an example of matches from the “fern” scene. Even with confidence filtering, due to domain shifts between training and testing, incorrect matches still persist. This is a common drawback of correspondence methods [33].

As presented in Table 4, multi-view supervision degrades performance. While the method has consistently worked on slower-converging NeRF, we believe INGP’s aggressive optimization dynamics will amplify supervision of incorrect matches, leading to sub-optimal results than our frequency supervision, which does not require pre-trained weights as priors. We hope our results encourage fellow researchers to re-adapt and re-think correspondence methods for fast-converging representations like INGP and 3DGS [15].

11. Frequency supervision in novel poses

It can be advantageous to perform supervisions on novel poses [11]. In the end, the task is *novel* view synthesis. Therefore, we tried extending the DW loss to novel poses:

$$\mathcal{L}_{DW} = \sum_{sb \in \{LL, LH, HL, HH\}} \lambda_{sb} \|\mathbf{I}^{sb}(\hat{\mathbf{p}}) - \tilde{\mathbf{I}}_{gt}^{sb}(\hat{\mathbf{p}})\|_2^2$$

where $\hat{\mathbf{p}}$ is an interpolated view from a sampled pair of known poses $\{\mathbf{p}_0, \mathbf{p}_1\}$, similar to our implementation of DietNeRF. $\tilde{\mathbf{I}}_{gt}^{sb}(\hat{\mathbf{p}})$ is the pseudo ground-truth sub-band at novel view $\hat{\mathbf{p}}$. Inspired by GeCoNeRF [17] and SfMLearner [?], we obtained $\tilde{\mathbf{I}}_{gt}^{sb}(\hat{\mathbf{p}})$ as follows:

$$\tilde{\mathbf{I}}_{gt}^{sb}(\hat{\mathbf{p}}) = \text{DWT}[\tilde{\mathbf{I}}_{gt}(\hat{\mathbf{p}})] = \text{DWT}\{\text{sampler}[\mathbf{I}_{gt}(\mathbf{p}), \mathbf{x}_{\hat{\mathbf{p}} \rightarrow \mathbf{p}}]\}$$

where $\text{DWT}\{\cdot\}$ is the Discrete Wavelet Transform, operating on $\tilde{\mathbf{I}}_{gt}(\hat{\mathbf{p}})$. The $\text{sampler}[\cdot, \cdot]$ applies bilinear interpolation to retrieve the warped pixel values from the actual ground-truth view at known pose \mathbf{p} , $\mathbf{I}_{gt}(\mathbf{p})$, at the projected coordinates $\mathbf{x}_{\hat{\mathbf{p}} \rightarrow \mathbf{p}}$:

$$\mathbf{x}_{\hat{\mathbf{p}} \rightarrow \mathbf{p}} = \mathbf{K} \mathbf{T}_{\hat{\mathbf{p}} \rightarrow \mathbf{p}} \mathbf{D}(\hat{\mathbf{p}}) \mathbf{K}^{-1} \mathbf{x}_{\hat{\mathbf{p}}}$$

where \mathbf{K} is the known camera intrinsic matrix, $\mathbf{T}_{\hat{\mathbf{p}} \rightarrow \mathbf{p}}$ is the camera transformation matrix from the novel to known poses, $\mathbf{D}(\hat{\mathbf{p}})$ is the predicted depth map at the novel pose (naturally available as part of the rendering process) and $\mathbf{x}_{\hat{\mathbf{p}}}$ are pixel coordinates in the novel pose. Figure 10 shows a visual example of this warping process.

Implementation Details We again replace the Vanilla DW loss with the “Novel” DW loss in Algorithm 1, and kept all other hyperparameters intact. The warping process will introduce black regions due to out-of-bounds sampling, but we simply did not consider them in the loss calculation.

Table 7 shows the results. The DW loss, operating on novel poses, still outperforms the baseline, but performance

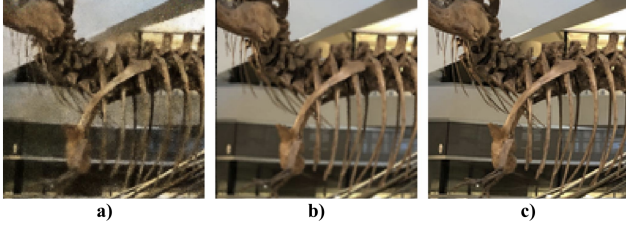


Figure 10. Differentiable image warping: (a) rendered view at novel pose $\hat{\mathbf{p}}$, (b) its pseudo ground-truth view, which is warped from c), actual ground-truth view at known pose \mathbf{p} . The warping allows supervision in novel poses.

is worse than operating on known poses. We hypothesize this is because warping errors corrupt the frequency supervision, and because out-of-bounds points reduce information for supervision. Future works could explore integrating the semantic (which works well at novel poses) and frequency supervision (which does not). For example, if an object is what it is regardless of viewing direction, so are its low and middle frequencies (like edges). This is unlike high frequencies, which are much more vulnerable to changes in viewing directions. This could be an interesting direction of frequency supervision. In the meantime, this experiment shows that the DW loss does not require operating on novel poses, thereby maintaining its ease of implementation.

Table 7. Ablation on DW loss in novel poses

METHOD	PSNR (\uparrow)	SSIM (\uparrow)	LPIPS (\downarrow)
COMBiNeRF (BASELINE)	20.12	0.676	0.197
DWTNeRF (w/ KNOWN DW.)	20.38	0.677	0.193
DWTNeRF (w/ NOVEL DW.)	20.22	0.669	0.194

12. Frequency decomposition levels

Table 5 shows results for 1-level decomposition, where the DWT is applied once to provide the sub-bands. However, we can take the resulting LL sub-band and similarly decompose it into another set of 4 sub-bands:

$$\begin{aligned} \mathbf{I}_2^{LL} &= \mathbf{L}\mathbf{I}^{LL}\mathbf{L}^T; \mathbf{I}_2^{LH} = \mathbf{H}\mathbf{I}^{LL}\mathbf{L}^T \\ \mathbf{I}_2^{HL} &= \mathbf{L}\mathbf{I}^{LL}\mathbf{H}^T; \mathbf{I}_2^{HH} = \mathbf{H}\mathbf{I}^{LL}\mathbf{H}^T \end{aligned}$$

where $\mathbf{I}_2^{(\cdot)}$ represent the 2-level decomposition of the sub-bands. $\mathbf{I}^{LL} = \mathbf{L}\mathbf{I}\mathbf{L}^T$ is the LL sub-band from 1-level decomposition. The remaining 1-level sub-bands are left intact. By further decomposing the LL sub-band, we can better enable the multi-resolution analysis characteristic of

Table 8. Ablation on wavelet decomposition levels

METHOD	PSNR (\uparrow)	SSIM (\uparrow)	LPIPS (\downarrow)
COMBiNeRF (BASELINE)	20.12	0.676	0.197
DWTNeRF (+DW. / HAAR - 1-LVL)	20.25	0.677	0.193
DWTNeRF (+DW. / HAAR - 2-LVL)	20.21	0.677	0.194

the DWT. Theoretically, this allows the representation of the scene at progressively coarser resolutions, enabling a hierarchical understanding of the scene’s structure. However, this is hard to implement. 1-level decomposed sub-bands are 4 times smaller than the original image. 2-level sub-bands are 8 times smaller, and so on. To ensure the sub-bands are still visually meaningful, and thus provide useful supervision, the original image has to be larger. As explained, this requires sampling a higher number of rays, making the method computationally expensive. For now, we conducted a simple experiment that used the 2-level decomposed sub-bands instead of 1-level in Algorithm 1. To keep the method computationally simple, we retained the patch-based sample batch size $|\mathcal{R}_P|$ used in the 1-level experiment. Figure 11 shows the decomposed scenes. 2-level decomposition loses finer details, but pushes the details to the forefront, so it’s worth investigating. Table 8 shows the results. While using 2-level still outperforms the baseline, the results are worse than 1-level. This confirms our intuition that the DW loss needs visually meaningful features. However, future works could introduce an efficient procedure to allow a multi-level, hierarchical DW loss that is more in line with multi-resolution analysis.

13. Model methods

In previous sections, we established the advantages of DWTNeRF’s DW loss over two prevalent prior-based losses, while validating the design choices. In this section, we compared DWTNeRF’s cross-branch interactions against model methods as introduced by mi-MLP [46]: “Residual Connections” and “Element-wise Cross-branch Interactions”. The architectures of each method are provided in Figure 6. In general, model methods aim to boost few-shot NeRF by tweaking Vanilla MLP’s architecture.

Network Structures Following CombiNeRF [2] and mi-MLP [46], DWTNeRF is modelled using separate MLP branches for densities and colors. The density branch has 2 MLP layers, and its inputs are encoded using hash encoding [22] with 16 resolution levels. The color branch has 3 MLP layers, and its inputs are encoded using 64 bases of the spherical harmonics [27].

Residual Connections This provides a shorter path between the inputs and intermediate MLP layers, helping to reduce overfitting. For our implementation onto INGP, we

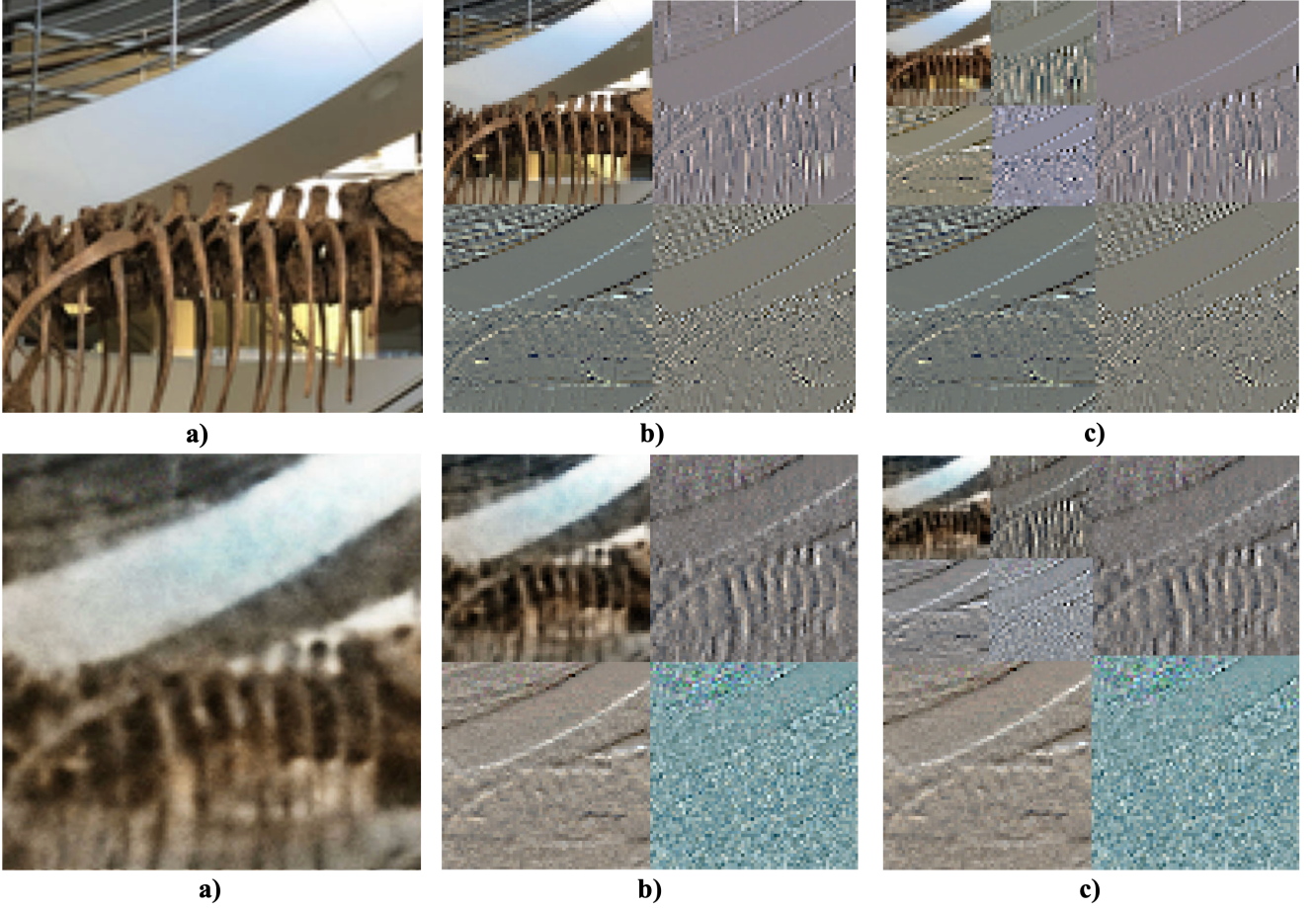


Figure 11. Multi-level decompositions. The top row is for the ground-truth view, the bottom for the rendered view. From left to right: a) original image, b) 1-level decomposition and c) 2-level. Moving from b) to c), only the LL sub-band is decomposed further, while the remaining sub-bands are kept intact.

introduced the residuals with the concatenation operator $[\cdot, \cdot]$:

$$f_i = \text{Linear}([f_{i-1}, \gamma(\cdot)])$$

where `Linear` is Pytorch’s `Linear` layer. f_i and f_{i-1} denote the outputs of the i -th layer and the layer preceding it. The encoded inputs $\gamma(\cdot)$ are either $\gamma(\mathbf{x})$ or $\gamma(\mathbf{d})$, depending on the MLP branch. We implemented residuals for both branches, up until the penultimate layer.

Element-wise Cross-branch Interactions This provides interactions between color and density branches, regularizing color predictions through position-aware relationships. We implemented this into INGP as follows:

$$f_i^{\mathbf{d}} = \text{Linear}_1[f_{i-1}^{\mathbf{d}} + \text{Linear}_2(f_{i-1}^{\mathbf{x}})]$$

where $f_i^{\mathbf{d}}$ and $f_i^{\mathbf{x}}$ denote the i -th layer at the color and density branches, respectively. The second linear layer,

`Linear2`, is to ensure similar dimensions between the intermediate features from each branch for element-wise addition. The interaction is one-way (i.e., from the density towards the color branch, but not vice versa) to keep the density features lean. This is because densities are only position-dependent, and are vulnerable to over-parameterization.

As presented in Table 4, all of the above methods degrade performance. Similar to some prior methods, model methods are not trivially transferable across Vanilla NeRF and INGP, and very possibly, 3DGS. This is due to INGP’s aggressive optimization dynamics, making it vulnerable to very slight architectural changes. Our method, based on multi-head attention and acting only on the inputs & outputs, bypasses this shortcoming while still capable of learning density-color interactions.

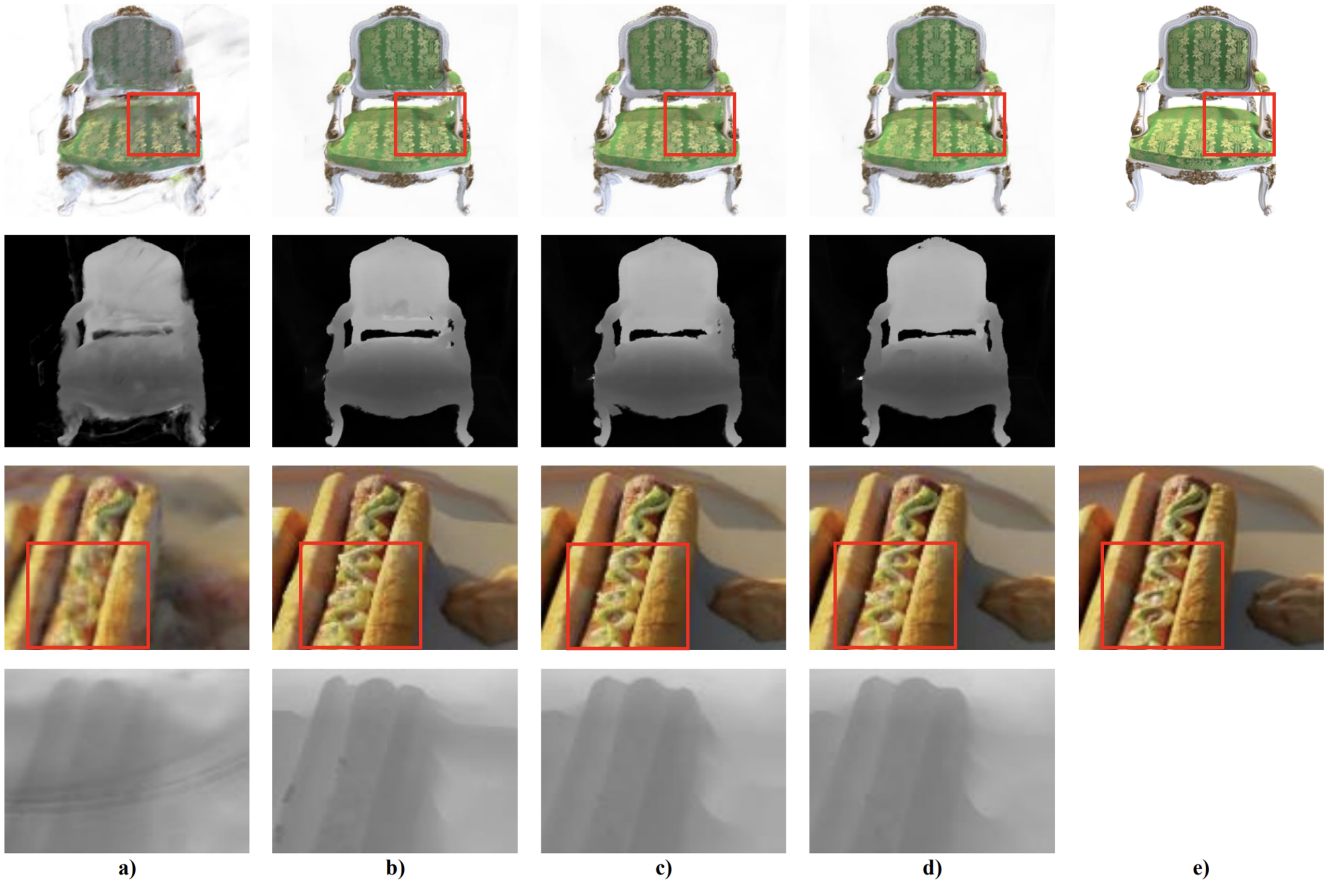


Figure 12. Qualitative results for Vanilla INGP (a), CombiNeRF (b), DWTNeRF with only cross-branch interactions (c), DWTNeRF with full modules (d) and ground-truth (e) on the NeRF-Synthetic [21] dataset (“chair” and “hotdog” scenes)

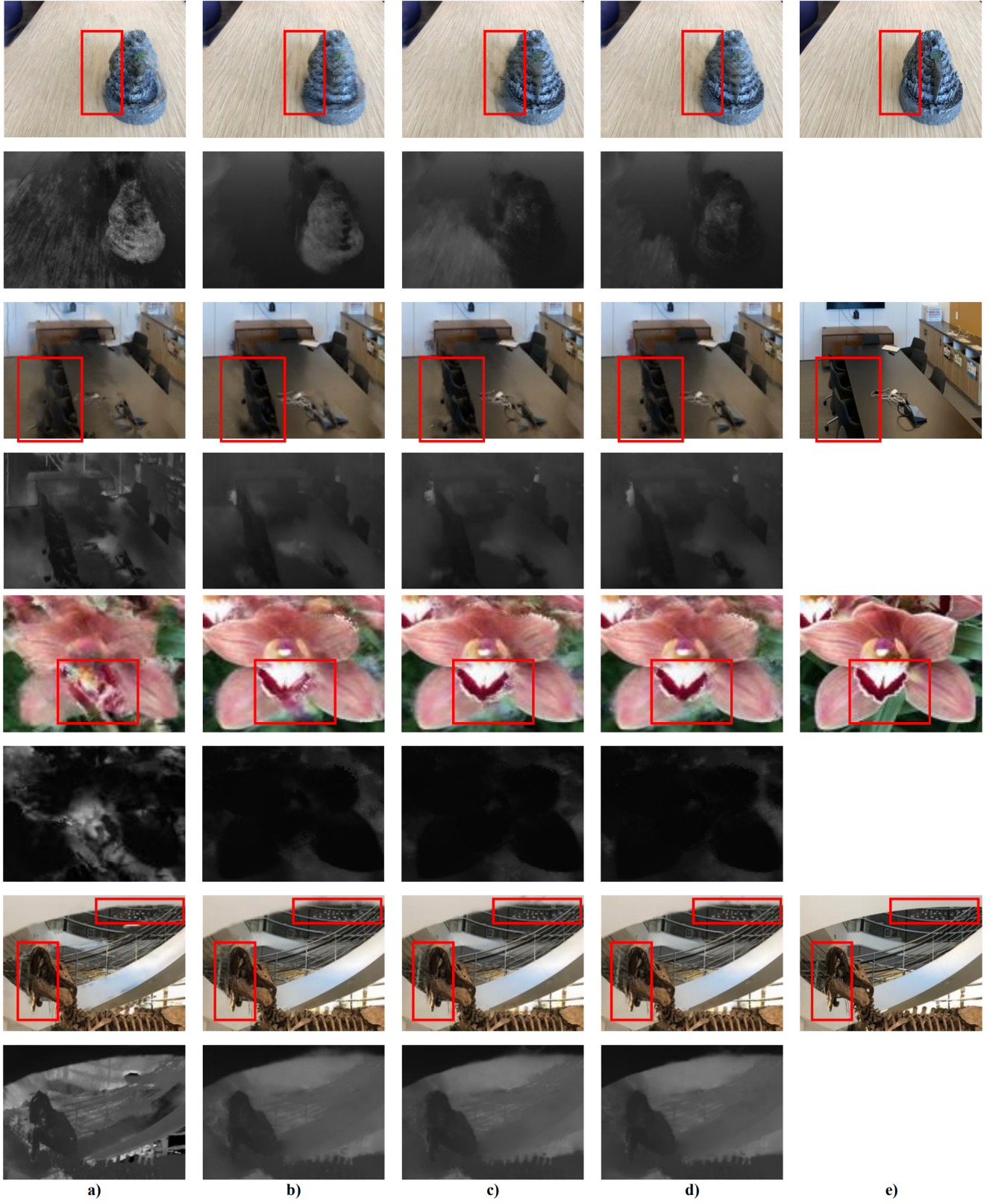


Figure 13. Qualitative results for Vanilla INGP (a), CombiNeRF (b), DWTNeRF with only cross-branch interactions (c), DWTNeRF with full modules (d) and ground-truth (e) on the LLFF [20] dataset. Upper row depicts the novel views, while lower row depicts the corresponding depth maps. From top to bottom: “fortress”, “room”, “orchids” and “trex” scenes. The **red** regions show improved visual qualities.